Regionally optimized fire parameterizations using feed-forward neural networks

Yoo-Geun Ham[1*], Seung-Ho Nam[2], Geun-Hyeong Kang[2], and Jin-Soo Kim[3*]

[1] Department of Environmental Planning, Graduate School of Environmental Studies, Seoul National University, Seoul, South Korea

[2] Department of Oceanography, Chonnam National University, Gwangju, 61186, South Korea

[3] Low-Carbon and Climate Impact Research Centre, School of Energy and Environment, City University of Hong Kong, Tat Chee Ave, Kowloon Tong, Hong Kong, People's Republic of China

Correspondence to: Prof. Yoo-Geun Ham (yoogeun@snu.ac.kr), and Prof. Jin-Soo Kim (jinsoo.kim@cityu.edu.hk)

The fire weather index (FWI) is a widely used metric for fire danger based on meteorological observations. However, due to its empirical formulation based on a specific regional relationship between the meteorological observations and fire intensity, the ability of the FWI to accurately represent global satellite-derived fire intensity observations is limited. In this study, we propose a fire parameterization method using feed-forward neural networks (FFNNs) for individual grids. These FFNNs for each grid point utilize four daily meteorological variables (2-meter relative humidity (RH2m), precipitation, 2-meter temperature, and wind speed) as inputs. The outputs of the FFNNs are satellite-derived fire radiative power (FRP) values. Applying the proposed FFNNs for fire parameterization during the 2001–2020 period revealed a marked enhancement in cross-validated skill compared to parameterization solely based on the FWI. This improvement was particularly notable across East Asia, Russia, the eastern US, southern South America, and central Africa. The sensitivity experiments demonstrated that the RH2m is the most critical variable in estimating the FRP and its regional differences via the FFNNs. Conversely, the FWI-based estimations were primarily influenced by precipitation. The FFNNs accurately captured the observed nonlinear RH2m-FRP and precipitation-FRP relationship compared to that simulated in the FWI-based model.

Keywords: fire parameterization, fire radiative power, fire weather index, feed-forward neural networks

1. Introduction

Wildfires are inflicting substantial terrestrial and economic impacts in numerous regions globally (Bowman et al., 2009). For example, In 2020, the United States experienced a total of US$16.5 billion in damages due to wildfires, with over 10,000 structures in California alone being damaged or completely destroyed (NOAA, 2021). The 2019-2020 wildfire season in Australia was exceptionally severe, causing smoke-related health costs of AU$1.95 billion, including an estimated 429 premature deaths and over 4,700 hospital visits, a cost nearly nine times the median annual cost of AU$211 million over the previous 19 years (Johnston et al., 2021). Therefore, monitoring and managing the risk of fire incidents at an early stage poses a significant challenge for each country in reducing casualties and economic losses (Vitolo et al., 2019).

As fire propagation is mainly determined by dryness after its ignition, spatially estimating and forecasting dryness enables the monitoring of fire hazards (Bistinas et al., 2014, Abatzoglou and Williams 2016). Facilitating the implementation of emergency measures to curb the expansion of uncontrollable large fires (Di Giuseppe et al., 2016, Bett et al., 2020, Haas et al., 2022). For this reason, in order to prevent fires, various techniques for quantifying and monitoring dryness have been developed and are being used. Indeed, the European Centre for Medium-Range Weather Forecasts (ECMWF) provides the Canadian Forest Fire Weather Index, the Australian McArthur Forest Fire Danger Index, and the Keetch-Byram Drought Index through the European Forest Fire Information System (EFFIS).

Among several operational fire danger indices, the Fire Weather Index (FWI) holds a prominent status as an indicator of potential fire intensity. Developed by the Canadian Forest Fire Danger Rating System (Van Wagner 1974, 1987), the FWI is based on four daily meteorological observations: near-surface air temperature, near-surface air relative humidity, wind speed, and precipitation. Fuel moisture codes are first determined from meteorological data to assign numerical ratings to the moisture content of the forest floor and other deceased organic matter. Afterward, the moisture codes are provided as an input of the fire behavior indices, such as the initial spread index and buildup index, to finally calculate the FWI, providing an estimation of wildfire intensity under given meteorological conditions (Vitolo et al., 2019).

Although this system has been shown to be globally applicable (Bedia et al., 2015, Abatzoglou et al., 2018), it was originally developed for the characterization of evergreen pine stands in forested areas of Canada. Therefore, all links between fire moisture codes and fire behavior indices are optimized and parameterized for eastern Canada. However, regional fire dynamics vary significantly depending on its unique climatological states (Flannigan et al., 2005, Kim et al., 2019). For example, extensive deforestation fires in the Amazon are attributed to insufficient cumulative precipitation (Le Page et al., 2010), whereas Arctic fire activity is more sensitive to temperature and relevant timing of snowmelt (Kim et al., 2020); however, its regional differences would not be fully considered as the strength of FWI which is originally optimized and derived for physical characteristics of Canadian fire, while the relationship between the meteorological conditions and the fire activity varies significantly from regions to regions.

Artificial neural networks (ANN) have recently received extensive attention and continue expanding to various application fields, including wildfire research. The traditional ANN model with shallow neural networks, such as multilayer perceptron, and convolutional neural networks has been applied to predict the fire probability over the regional domain (Satir et al., 2016), or parameterize the fire occurrence (Zhang et al., 2021) from the meteorological variables. Despite previous literature demonstrating promising accuracy in estimating or predicting fire characteristics, the development of globally applicable ANN-based parameterization is still in its early stages. This is primarily due to the regional idiosyncrasies in the relationships between meteorological variables and fire activity, posing challenges for establishing global implementation.

To understand the varying sensitivities of wildfire activity to the meteorological variables from different regions, our study optimized fire parameterizations with satellite-derived fire radiative power (FRP) datasets based on feed-forward neural networks (FFNNs) in each region with fire activity records. Given that FFNNs follow the same structure and input variables as the FWI, the parameter values linking meteorological observations, fuel moisture code, and fire behavior indices are established for every 1° × 1° resolution grid box via FFNNs, thus foregoing raw parameterizations in the Canadian FWI. In addition to our novel FFNN-based model, we also conducted an in-depth examination of the FWI-based model with FRP for comparative purposes. To quantify the relative contributions of each meteorological parameter to the fire parameterizations, sensitivity experiments were conducted based on climatological values of meteorological observations.

2. Data and Experimental Design

2.1. Data

2.1.1. Fire radiative power (FRP)

Given that the FWI was designed to estimate potential fire intensity, our analyses were based on satellite-derived FRP, a metric that represents the rate at which a fire emits energy in the form of thermal radiation. Specifically, daily FRP data was sourced from the Moderate Resolution Imaging Spectroradiometer (MODIS) Collection 6.1 dataset provided by the Fire Information for Resource Management System (FIRMS) (https://firms.modaps.eosdis.nasa.gov/active_fire/) (Giglio et al., 2016). The period of the FRP data spans from 2001 to 2020. The dataset featured a spatial resolution of 1°×1° across the entire globe (0°–360°E, 90°S–90°N), with values expressed in megawatts (10^6 J s^{-1}; MW). It is important to note that although products were generated for both land and ocean areas, we exclusively focused on land values, as FRP is directly associated with fire size and intensity over terrestrial surfaces.

2.1.2. Meteorological observations

Meteorological observations are required as an input of the FWI and the FFNNs for the FRP parameterizations. In this study, we used daily-averaged 2 m air temperature (T2m), 2 m air relative humidity (RH2m), 10 m wind speed (WS10m), and precipitation (PRCP) from ERA5 reanalysis produced by the European Centre for Medium-Range Weather Forecasts (ECMWF) from 2001 to 2020 (Hersbach et al., 2020). The original horizontal resolution was a quarter degree but was interpolated to a 1°×1° resolution over the entire globe (0°–360°E, 90°S–90°N).

2.2. Models

2.2.1. FWI-based model

A FRP-estimation model based on the FWI was established as a baseline. The FWI is obtained from the daily averages of T2m, RH2m, WS10m, and PRCP, and the source code to produce the FWI was obtained from the Canadian Forest Service at https://cfs.nrcan.gc.ca/publications/download-pdf/36461. To match the systematic amplitude differences between the FWI and FRP using the different units, a linear regression coefficient of the FRP with respect to the FWI, which was separately calculated for each grid point, is multiplied to produce the FWI-based model. Therefore, the nonlinearity between the meteorological variable and the FRP in the baseline model is purely originated from the procedure to derive the FWI. A cross-validation strategy was adopted for the skill assessment. For more details, please refer to section 2.3.

2.2.2. FFNNs for FRP parameterization

The FFNNs employed for FRP parameterization consist of one input layer, three hidden layers, and one output layer (Figure 1). The input layer comprises four neurons corresponding to daily averages of T2m, RH2m, WS10m, and PRCP at a specific grid point. The output layer, on the other hand, encompasses a single neuron respresening concurrent FRP estimation at the corresponding grid point. Notably, FFNNs are configured individually for each grid point. The first, second, and third hidden layers are composed of 64, 32, and 16 neurons, respectively. Activation functions are implemented utilizing the ReLU function, which is known to be powerful by introducing nonlinearity and solving the vanishing gradient issues (Agarap, 2018). Techniques such as batch normalization to normalize activations in intermediate layers of deep neural networks (Bjorck et al., 2018), and dropout to prevent an overfitting to the training data by randonmly drop units (Srivastava et al., 2014) with a dropout rate of 0.2, are applied to enhance model robustness.

It should be noted that the meteorological observations serving as input for the FFNNs mirror those employed in the FWI. Thus, any disparities in estimation accuracy between the FFNNs and the FWI-based model solely stem from the FRP estimation algorithm.

The loss function of the FFNNs is defined as the root-mean-squared difference between the observed FRP (y) and the estimated FRP ($\hat{\mathrm{y}}$) as follows.

$$\mathrm{Loss} = \sum_{n=1}^{N} (\mathrm{y_n} - \widehat{\mathrm{y_n}})^2$$

where N denotes the number of training samples. Total numer of epochs for the traininng is set to 1,000, and early stopping is applied (Raskutti et al., 2014), once the validation loss is not decreased for 100 epoches. It is shown that both the training and validation loss is decreased with the increased epoch (Supplementary Fig. S1), indicating that the FFNNs to estimate the FRP are successfully formulated. Similar to the FWI-based model, a cross-validation strategy is adapted for the skill assessment (see section 2.3 for more details).

2.3. Cross-validation strategy for the skill assessment

The performance of both the FFNNs and the FWI-based model was assessed by adopting a cross-validation strategy. The dataset was partitioned into distinct subsets for testing, validation, and training purposes. The testing period was defined by dividing the entire period from 2001 to 2020 into four-year intervals. The validation dataset is defined as the last two years of each four-year interval, whereas the remaining data was used for training. For example, for the 1st Jan. 2001–31st Dec. 2004 test period, the models were trained using a 1st Jan. 2005– 31st Dec. 2018 dataset, whereas the data from 1st Jan. 2019– 31st Dec. 2020 was used for validation. Additional details on the selection of periods for training, validation, and testing are provided in Supplementary Table S1. After aligning all testing results from multiple sets of experiments with different period for training/validating/testing, the skill in estimating FRP was estimated using both FFNNs and FWI-based models across the 2001–2020 period. We note that evaluating the skill of FFNN against FRP data may lead to an overestimation of its estimation abilities, given that the FFNN is trained using same type of data. Regrettably, the absence of ground-based observations on fire activity/intensity for the enough period deprives us of the opportunity to cross-reference FFNN-based FRP estimations with independent observations. The FRP anomalies, which were calculated by subtracting the estimated daily climatology during 2001–2020 period, were compared and assessed for the FRP estimation accuracy.

3. FRP parameterization using the FFNNs

Figure 2 illustrates the correlation skill and root-mean-squared error (RMSE) between the observed FRP anomalies from 2001 to 2020 and the FRP anomalies estimated with FFNNs and the FWI-based model. The correlation skill of the FFNNs exceeded 0.6 over southern China, northern India, southern South America, the eastern US, southern Africa, western-central Russia, and maritime continents (Figure 2a). In contrast, the correlation skill of the FWI-based model fell below 0.6, with southern China and central Africa being the only exceptions (Figure 2b). Therefore, the FFNNs consistently exhibited superior correlation skills compared to the FWI-based model over most of the globe (Figure 2c). Notably, the improvement in the correlation skill of the FFNNs was statistically significant at a 95% confidence level, as determined using the method outlined by Zou (2007). This significance was particularly pronounced over East Asia, the entirety of Russia, the eastern US, southern South America, and central Africa.

The RMSE of the FRP estimations tended to be higher over the regions with high FRP climatology in both models (Supplementary Fig. S2). A clear distinction in the RMSE emerges upon comparing FFNNs and the FWI-based model; FFNNs demonstrate an RMSE below 1.5 MW across most regions (Figure 2d), while the FWI-based model predominantly registers RMSE values ranging between 1.5 and 1.8 MW (Figure 2e). Consequently, the global depiction of RMSE differences reveals negative values, illustrating the consistent superiority of FFNNs over the FWI-based model (Figure 2f).

The systematic improvement in the accuracy of the estimated FRP using the FFNNs was consistently robust when the skill is evaluated after excluding non-wildfire events (i.e., skill evaluation only when observed FRP > 0) (Supplementary Fig. S3) or when considering monthly-averaged FRP anomalies (Supplementary Fig. S4); both estimation of the fire events in daily scale and its interannual variations of the FRPs with FFNNs align more closely with the observed FRPs than the corresponding outputs of the FWI-based model.

To examine the realism of the temporal variation of the estimated FRP in more detail, Figure 3 shows time-series of the yearly-averaged observed and estimated FRP over Brazil (Figure 3a), Africa (Figure 3b), Siberia (Figure 3c), and Southern China (Figure 3d). The correlation skill across the various regions consistently exhibited higher correlation skill. Interestingly, the daily evolution and its intensity estimation for the record-breaking wildfire events over the Brazil in 2019 (Brando et al., 2020) (Figure 3e), Africa in 2016 (Verhegghen et al., 2016) (Figure 3f), Siberia in 2003 (Huang et al., 2009) (Figure 3g), and southern China in 2007 (Cao et al., 2017) (Figure 3h) are consistently better estimated in the FFNNs. These findings highlight the superiority of FFNNs over the FWI-based model not only in estimating overall variations of the fire intensity, and its detailed evolution and intensity of record-breaking wildfire event worldwide by successfully exploring the relationship between the FRP and the meteorological observations.

To identify the main factors that contributed to the superior accuracy of the FFNNs, sensitivity experiments were conducted by fixing one of the meteorological observations to the daily climatological values (Figure 4); for example, in the RH2m Clim experiment, the prescribed values of RH2m as an input of the FFNN is the daily climatology during the whole period (i.e., 2001-2020), therefore, its year-to-year variations in the RH2m is removed. Then, the correlation skill difference between the control simulation, that prescribes all input values at the corresponding date, and the RH2m Clim experiment is calculated to assess the importance of the RH2m in FRP parameterization. It clearly indicates that the RH2m are the main factors influencing the accuracy of the FRP estimations in the FFNNs. For example, the correlation skill difference between the original estimation and the estimation with the climatological RH2m was close to 0.5 over most of the regions where the original FRP estimations exhibited high skill (Figure 4a). On the other hand, substituting PRCP with its climatological value had a negligible impact on the FFNN-based approach (Figure 4b). Therefore, RH2m was the dominant variable influencing FRP estimations via the FFNNs method over most of the globe except for a few regions (Figure 4c). The correlation skill also remained relatively unaffected when daily climatological values of WS10m, T2m were considered for the FRP estimations using the FFNNs (Supplementary Fig. S5).

Conversely, when employing the FWI-based model, the alteration in FRP correlation skill is more pronounced upon substituting PRCP with its daily climatological values. In regions such as southern China, northern India, southeastern South America, and the eastern US, the correlation skill decrease is between 0.2 and 0.3 due to this substitution. In contrast, replacing RH2m with its climatology results in correlation skill differences of less than 0.1 (Figure 4d and 4e). These findings underscore the importance of PRCP as the meteorological variable with the greatest influence on FRP estimation using the FWI (Figure 4f). The correlation skill also remained relatively unaffected when daily climatological values of WS10m, T2m were considered for the FRP estimations (Supplementary Fig. S6).

To support our arguments that the RH2m is most importance factor in the FFNNs, we adapted the layer-wise relevance propagation (LRP) technique (Bach et al., 2015; Barns et al., 2020; Toms et al., 2020), which is widely used for understanding the relevance of individual features or neurons in neural networks. It provides a so-called relevance score R for each variable, which linearly decompose the importance of each input variables as follows by propagating the output value backward toward the input variables using a chain rule.

$$f(RH2m, PRCP, T2m, WS10m) = R_{RH2m} + R_{PRCP} + R_{T2m} + R_{WS10m}$$

where f is a nonlinear model (i.e., FFNNs) to derive the FRP, and R_{RH2m}, R_{PRCP}, R_{T2m}, R_{WS10m} is a relevance score of RH2m, PRCP, T2m, and WS10m, respectively. The relative importance of any particular variable to the estimated FRP can be quantified by calculating the degree of the similarity between the output value and the relevance scores. For this purpose, we obtained the relevance score of each variable for each day during the whole testing period (i.e., 2001-2020) and calculated the correlation with the estimated FRP in the FFNNs (Figure 5). This analysis supports our previous notion that the RH2m is the most sensitive factor influencing FRP estimation in FFNNs, with the contributions of other meteorological parameters being comparatively minor.

The dramatic disparity in the relative contributions of RH2m and PRCP between the two models indicates that the factors that drive the predictive performance of the two models were different. Therefore, the relationship between these two key meteorological observations and the FRP estimations will be further explored in the next section to gain insights into the factors that determine the superior performance of the FFNN-based approach.

4. Physical explanations of the superior performance of FFNNs

To confirm that the superior performance of the FFNNs is associated with the differences in the relationship between the RH2m and the estimated FRP between the FFNNs and the FWI-based models, we selected grid points that satisfy the following three conditions: (1) an FRP correlation skill improvement in FFNNs over FWI-based models is greater than a threshold value (i.e., 0.05 in this case), (2) RH2m is the most sensitive variable for FRP estimation in FFNNs (green color in Fig. 2c), and (3) PRCP is the most sensitive variable in the FWI-based model (blue color in Fig. 2f). A total of 852 grid points were selected based on these criteria, which accounts for approximately 25.1% of total land grid points and 49.7% of total grid points whose correlation skill improvement in the FFNNs is greater than a threshold value of 0.05. The selected grid points are located over southern China, Russia, central Africa, the eastern US, and central-northern South America (Figure 6a). We note that a threshold of 0.1 for correlation skill improvement would not change the general conclusion, which will be discussed in the following paragraph.

Figure 6b-g illustrates the averaged FRP for each RH2m bin with a 10% interval. Our findings indicated that FRP exhibits a decrease when RH2m surpasses 30% (Figure 6b). Therefore, the difference in the FRP values in the higher RH2m bin from that in the lower RH2m bin exhibited negative values (Figure 6c). This relationship reflects the well-known impact of relative humidity on combustion (Papagiannaki et al., 2020;

Ying et al., 2021), as oxygen availability is constrained, resulting in reduced combustion rate and lowered FRP. Additionally, higher humidity can indicate the presence of moisture in the fuel, such as plants or other vegetation, thereby impeding fire propagation and further decreasing the FRP values.

Interestingly, in instances where RH2m falls below 30%, FRP tends to increase with higher RH2m values. Although this proportional relationship between relative humidity and fire activity is relatively uncommon, it can be occurred over the fuel-limited landscape, or the regions of following extended periods of drought or low humidity; Abatzoglou and Kolden (2013) showed that the positive correlation between the soil moisture and the burned area is enhanced in non-forested regions. This is similarly found in Xystrakis et al. (2014), which argued that the increased precipitation is associated with the build-up of the fuel, which eventually contribute to increase the burned area.

The FFNNs accurately simulated the aforementioned nonlinear relationship between the RH2m and the FRP (Figure 6d and 6e). In cases where RH2m < 30%, FRP increases with rising RH2m; for RH2m > 30%, FRP diminishes as RH2m rises. The consistency between the estimated and observed FRP values at each bin further supports our previous results, demonstrating the successful application of FFNNs in FRP parameterization.

In contrast, the FWI-based FRP estimations exhibit a linear inverse relationship between the RH2m and the FRP. Specifically, FRP decreases continuously with increasing RH2m (Figures 6f and 6g). This unrealistic representation, particularly in dry regimes, demonstrates that the observed nonlinear RH2m-FRP relationship was not faithfully captured in the FWI-based model. Furthermore, the FWI-based estimations tended to overestimate FRP in low RH2m bins (i.e., RH2m < 30%) and underestimate it in high RH2m bins (i.e., RH2m > 60%), which underscores the systematic biases in the FRP estimations in the FWI-based model.

Next, we assessed the relationship between daily-averaged PRCP and the FRP values (Figure 7). In both the observed FRP values and those estimated using FFNNs and FWI-based models, PRCP tended to inhibit fire events, causing FRP values to decrease with rising PRCP (Parks et al., 2014; Chen et al. 2014; Holden et al., 2018). In the observational data (Figure 7a), FRP reaches its maximum at 1.9 MW within the lowest PRCP bin (i.e., PRCP < 0.1 mm/day), after which it sharply decreases to approximately 1 MW in the subsequent bin (i.e., 0.1 mm/day < PRCP < 0.2 mm/day).

Afterward, it experiences a gradual decrease with increasing PRCP when PRCP is below 3 mm/day. However, for PRCP values exceeding 3 mm/day, the extent to which FRP decreases with higher PRCP becomes less pronounced, as higher precipitation does not proportionally reduce ignition likelihood (Oliveras et al., 2014). This leads to sustained FRP values above a certain threshold (i.e., 0.5 MW) for PRCP > 3 mm/day. The spatially averaged FRP distribution in instances where PRCP > 3 mm/day maintains moderate values, ranging from 1 to 2 MW over regions such as Mexico, Colombia, central South America, central Africa, central Western Asia, Australia, and the maritime continent (Figure 7b).

FFNNs accurately simulated the observed relationship between the FRP and the PRCP, with the estimated FRP in FFNNs exhibiting high values within the smallest PRCP bins (approximately 1.75 MW), which decreased as PRCP increased when PRCP was below 3 mm/day (Figure 7c). The spatial distribution of the averaged FRP for the cases where PRCP > 3 mm/day was also similar to the observed values (Figure 7d). Conversely, FRP estimation in the FWI-based model tended to be underestimated, particularly in bins with higher PRCP (Figure 7e). For instance, bins with PRCP < 0.5 mm/day exhibited an underestimation of approximately 0.25 MW, whereas underestimations of over 0.5 MW, and nearly 0 MW, were evident when PRCP > 3 mm/day. This is further evidenced by the spatially averaged FRP distribution for PRCP > 3 mm/day, which is almost negligible worldwide (Figure 7f).

As a result, the regression coefficient between the FRP estimation and the PRCP is systematically greater in the FWI-based model. For observations, the quadratic coefficient is 0.022 MW/(mm/day)^2 (black in Figure 7a), and that for the FFNNs 0.023 MW/(mm/day)^2 (black in Figure 7c), denoting similar amplitude. On the other hand, the FWI-based model is 0.036 MW/(mm/day)^2, which is almost twice to that of the others (black in Figure 7e). This suggests that the FWI-based model is more responsive to changes in PRCP, resulting in a more pronounced FRP decrease with increasing PRCP. This excessive sensitivity in the estimated FRP to PRCP changes can contribute to the excessive influence of PRCP on the FRP estimations in the FWI-based model, as shown in Figure 4f.

5. Summary and Discussion

In this study, we developed a parameterization method using FFNNs to estimate global gridded FRP fields from meteorological variables. In the FFNNs, four daily meteorological observations, namely 2 m temperature, 2 m specific humidity, wind speed, and precipitation, were used as the input to predict the daily FRP output. The cross-validated FRP parameterization results during 2001–2020 exhibited an improved skill in estimating the observed FRP compared to the FWI-based model. The improvement in the parameterization accuracy in terms of the correlation skill and the RMSE was observed over most of the globe and was particularly prominent over East Asia, Russia, the eastern US, southern South America, and central Africa. This indicates that FFNNs can more effectively capture the nonlinear relationship between meteorological observations and FRP compared to the commonly employed fire index.

To identify the mechanism of the skill improvement in the FFNNs, a series of sensitivity experiments were performed by replacing each variable with the daily climatological values, and our findings demonstrated that the 2 m relative humidity (RH2m) was the most critical variable influencing the outcomes of the FFNNs over most of the globe. On the other hand, in the FWI-based model, PRCP plays a more substantial role in FRP estimation. The observed nonlinear relationship between the RH2m and the FRP is well simulated in the FFNNs; both the observation and the FFNNs exhibited a negative relationship in the wet regime (i.e., RH2m > 30%), whereas a positive relationship was observed in the dry regime (i.e., RH2m < 30%). Likewise, FFNNs accurately simulated the observed impact of PRCP on FRP reduction.

In contrast, the FWI-based model simulated a linear negative relationship between the FRP and the RH2m, which caused systematic errors in estimating the FRP, particularly in the dry regime. Moreover, the FWI-based model exaggerates the degree of FRP reduction with increasing PRCP, which contributes to the stronger contribution of PRCP to the FRP estimations compared to those obtained with the FFNNs. This discrepancy underscores the applicability of FFNNs in understanding the intricate relationship between meteorological observations and FRP, offering insights for refining the algorithm for global FWI calculations. While process-based fire models are valuable for estimating fire activity changes due to greenhouse gas warming, their performance is comparatively less robust compared to empirical models (Rabin et al., 2015; Hantson et al., 2016). Therefore, FFNN parameterizations could enhance process-based land surface models, yielding reliable fire activity predictions and insights into their evolution under greenhouse gas warming scenarios.

Current FFNNs solely leverage meteorological observations for FRP parameterization to ensure equitable comparison with the FWI-based model. However, the incorporation of land surface observations such as soil moisture could optimize FFNNs for simulating fire events more effectively. This provides an opportunity to reduce the significant uncertainties in predicting fire events in parameterizing fires in earth system models, ultimately mitigating potential losses from natural hazards.

References

Abatzoglou, J. T. and Kolden, C. A.: Relationships between climate and macroscale area burned in the western United States, Int. J. Wildland Fire, 22, 1003–1020, https://doi.org/ 10.1071/WF13019, 2013.

Abatzoglou, J. T. and Williams, A. P.: Impact of anthropogenic climate change on wildfire across western US forests, Proc. Natl. Acad. Sci. U.S.A., 113, 11770–11775, https://doi.org/10.1073/pnas.1607171113, 2016.

Abatzoglou, J. T., Williams, A. P., Boschetti, L., Zubkova, M., and Kolden, C. A.: Global patterns of interannual climate–fire relationships, Glob. Chang. Biol. 24, 5164–5175, https://doi.org/10.1111/gcb.14405, 2018.

Agarap, A. F. Deep learning using rectified linear units (relu). *arXiv preprint arXiv:1803.08375*, 2018.

Bach, S., Binder, A., Montavon, G., Klauschen, F., Müller, K.-R., and Samek, W.: On pixel-wise explanations for non-linear classifier decisions by layer-wise relevance propagation, PLoS One 10, 1–46, https://doi.org/10.1371/journal.pone.0130140, 2015

Barnes, E. A., Toms, B., Hurrell, J. W., Ebert-Uphoff, I., Anderson, C., and Anderson, D.: Indicator patterns of forced change learned by an artificial neural network, J. Adv. Model. Eart. Syst., 12, e2020MS002195, https://doi.org/10.1029/2020MS002195, 2020.

Bedia, J., Herrera, S., Gutiérrez, J. M., Benali, A., Brands, S., Mota, B., and Moreno, J. M.: Global patterns in the sensitivity of burned area to fire-weather: implications for climate change, Agric. For. Meteorol., 214, 369–79, https://doi.org/ 10.1016/j.agrformet.2015.09.002, 2015.

Bett, P. E., Williams, K. E., Burton, C., Scaife, A. A., Wiltshire, A. J., and Gilham, R.: Skillful seasonal prediction of key carbon cycle components: NPP and fire risk, Environ. Res. Commun., 2, 055002, https://doi.org/10.1088/2515-7620/ab8b29, 2020.

Bistinas, I., Harrison, S. P., Prentice, I. C., and Pereira, J. M. C.: Causal relationships versus emergent patterns in the global controls of fire frequency, Biogeosciences, 11, 5087–5101, https://doi.org/10.5194/bg-11-5087-2014, 2014.

Bowman, D. M., Balch, J. K., Artaxo, P., Bond, W. J., Carlson, J. M., Cochrane, M. A., ... & Pyne, S. J. (2009). Fire in the Earth system. *science*, *324*(5926), 481-484.

Brando, P., Macedo, M., Silvério, D., Rattis, L., Paolucci, L., Alencar, A., ... & Amorim, C. (2020). Amazon wildfires: Scenes from a foreseeable disaster. *Flora*, *268*, 151609.

Cao, Y., Wang, M., & Liu, K. (2017). Wildfire susceptibility assessment in Southern China: A comparison of multiple methods. *International Journal of Disaster Risk Science*, *8*, 164-181.

Bjorck, N., Gomes, C. P., Selman, B., & Weinberger, K. Q. (2018). Understanding batch normalization. *Advances in neural information processing systems*, *31*.

Chen, F., Niu, S., Tong, X., Zhao, J., Sun, Y., and He, T.: The impact of precipitation regimes on forest fires in Yunnan Province, Southwest China., Sci. World J., 2014, 326782, https://doi.org/10.1155/2014/326782, 2014.

Di Giuseppe, F., Rémy, S., Pappenberger, F., & Wetterhall, F.: Using the Fire Weather Index (FWI) to improve the estimation of fire emissions from fire radiative power (FRP) observations, Atmospheric Chem. Phys., 18, 5359–5370, https://doi.org/10.5194/acp-18-5359-2018, 2018.

Di Giuseppe, F., Pappenberger, F., Wetterhall, F., Krzeminski, B., Camia, A., Libertá, G., and San Miguel, J.: The potential predictability of fire danger provided by numerical weather prediction, J. Appl. Meteorol. Climatol., 55, 2469–2491, https://doi.org/ 10.1175/JAMC-D-15-0297.1, 2016.

Duncan, B. N., Martin, R. V., Staudt, A. C., Yevich, R., and Logan, J. A.: Interannual and seasonal variability of biomass burning emissions constrained by satellite observations, J. Geophys. Res., 108, 4100, https://doi.org/10.1029/2002JD002378, 2003.

Flannigan, M. D., Logan, K. A., Amiro, B. D., Skinner, W. R., and Stocks, B. J.: Future area burned in Canada, Clim. Change, 72, 1–16, https://doi.org/10.1007/s10584-005-5935-y, 2005.

Giglio, L., Schroeder, W., and Justice, C. O.: The collection 6 MODIS active fire detection algorithm and fire products. Remote Sensing of Environment, 178, 31–41, https://doi.org/10.1016/j.rse.2016.02.054, 2016.

Grillakis, M., Voulgarakis, A., Rovithakis, A., Seiradakis, K. D., Koutroulis, A., Field, R. D., Kasoar, M., Papadopoulos, A., and Lazaridis, M.: Climate drivers of global wildfire burned area, Environ. Res. Lett., 17, 045021, https://doi.org/10.1088/1748-9326/ac5fa1, 2022.

Haas, O., Prentice, I. C., and Harrison, S. P.: Global environmental controls on wildfire burnt area, size, and intensity, Environ. Res. Lett., 17, 065004, https://doi.org/10.1088/1748-9326/ac6a69, 2022.

Hantson, S., Arneth, A., Harrison, S. P., Kelley, D. I., Prentice, I. C., Rabin, S. S., Archibald, S., Mouillot, F., Arnold, S. R., Artaxo, P., Bachelet, D., Ciais, P., Forrest, M., Friedlingstein, P., Hickler, T., Kaplan, J. O., Kloster, S., Knorr, W., Lasslop, G., Li, F., Mangeon, S., Melton, J. R., Meyn, A., Sitch, S., Spessa, A., van der Werf, G. R., Voulgarakis, A., and Yue, C.: The status and challenge of global fire modelling, Biogeosciences, 13, 3359–3375, https://doi.org/10.5194/bg-13-3359-2016, 2016.

Hersbach, H., Bell, B., Berrisford, P., Hirahara, S., Horányi, A., Muñoz-Sabater, J., Nicolas, J., Peubey, C., Radu, R., Schepers, D., Simmons, A., Soci, C., Abdalla, S., Abellan, X., Balsamo, G., Bechtold, P., Biavati, G., Bidlot, J., Bonavita, M., De Chiara, G., Dahlgren, P., Dee, D., Diamantakis, M., Dragani, R., Flemming, J., Forbes, R., Fuentes, M., Geer, A., Haimberger, L., Healy, S., Hogan, R. J., Hóm, E., Janisková, M., Keeley, S., Laloyaux, P., Lopez, P., Lupu, C., Radnoti, G., de Rosnay, P., Rozum, I., Vamborg, F., Villaume, S., and Thépaut, J.-N.: The ERA5 Global Reanalysis, Q. J. Roy. Meteorol. Soc., 146, 1999–2049, https://doi.org/10.1002/qj.3803, 2020.

Holden, Z. A., Swanson, A., Luce, C. H., Jolly, W. M., Maneta, M., Oyler, J. W., Warren, D. A., Parsons, R., and Affleck, D.: Decreasing fire season precipitation increased recent western US forest wildfire activity, P. Natl. Acad. Sci. USA, 115, 201802316, https://doi.org/10.1073/pnas.1802316115, 2018.

Huang, S., Siegert, F., Goldammer, J. G., & Sukhinin, A. I. (2009). Satellite-derived 2003 wildfires in southern Siberia and their potential influence on carbon sequestration. *International Journal of Remote Sensing*, *30*(6), 1479-1492.

Johnston, F.H., Borchers-Arriagada, N., Morgan, G.G., Jalaludin, B., Palmer, A. J., Williamson, G. J., and Bowman, D. M. J. S.: Unprecedented health costs of smoke-related PM2.5 from the 2019–20 Australian megafires, Nat. Sustain., 4, 42–47, https://doi.org/10.1038/s41893-020-00610-5, 2021

Jones, M. W., Abatzoglou, J. T., Veraverbeke, S., Andela, N., Lasslop, G., Forkel, M., Smith, A. J. P., Burton, C., Betts, R. A., van der Werf, G. R., Sitch, S., Canadell, J. G., Santín, C., Kolden, C., Doerr, S. H., and Le Quéré, C.: Global and regional trends and drivers of fire under climate change, Rev. Geophys., 60, e2020RG000726, https://doi.org/10.1029/2020RG000726, 2022.

Kim, J. S., Jeong, S. J., Kug, J. S., and Williams, M.: Role of local air-sea interaction in fire activity over equatorial Asia, Geophys. Res. Lett., 46, 14789–14797, https://doi.org/10.1029/2019GL085943, 2019.

Kim, J. S., Kug, J. S., Jeong, S. J., Park, H., and Schaepman-Strub, G.: Extensive fires in southeastern Siberian permafrost linked to preceding Arctic Oscillation, Sci. Adv., 6, eaax3308, https://doi.org/10.1126/sciadv.aax3308, 2020.

Laurent, P., Mouillot, F., Moreno, M. V., Yue, C., and Ciais, P.: Varying relationships between fire radiative power and fire size at a global scale, Biogeosciences, 16, 275–288, https://doi.org/10.5194/bg-16-275-2019, 2019.

Le Page, Y., van der Werf, G. R., Morton, D. C., and Pereira, J. M. C.: Modeling fire-driven deforestation potential in Amazonia under current and projected climate conditions, J. Geophys. Res.-biogeosciences, 115, G03012, https://doi.org/10.1029/2009JG001190, 2010.

NOAA (Natl. Ocean. Atmos. Assoc.). 2021. Billion-dollar weather and climate disasters 2021. Natl. Cent. Environ. Inf., Natl. Ocean. Atmos. Assoc., Washington, DC. https://www.ncdc.noaa.gov/billions/

Oliveras, I., Anderson, L. O., and Malhi, Y.: Application of remote sensing to understanding fire regimes and biomass burning emissions of the tropical Andes, Global Biogeochem. Cy., 28, 480– 496, https://doi.org/10.1002/2013GB004664, 2014.

Papagiannaki, K., Giannaros, T. M., Lykoudis, S., Kotroni, V., & Lagouvardos, K. (2020). Weather-related thresholds for wildfire danger in a Mediterranean region: The case of Greece. Agricultural and Forest Meteorology, 291, 108076.

Parks, S. A., Parisien, M.-A., Miller, C., and Dobrowski, S. Z.: Fire Activity and Severity in the Western US Vary along Proxy Gradients Representing Fuel Amount and Fuel Moisture, PLoS ONE, 9, e99699, https://doi.org/10.1371/journal.pone.0099699, 2014.

Rabin, S. S., Melton, J. R., Lasslop, G., Bachelet, D., Forrest, M., Hantson, S., Kaplan, J. O., Li, F., Mangeon, S., Ward, D. S., Yue, C., Arora, V. K., Hickler, T., Kloster, S., Knorr, W., Nieradzik, L., Spessa, A., Folberth, G. A., Sheehan, T., Voulgarakis, A., Kelley, D. I., Prentice, I. C., Sitch, S., Harrison, S., and Arneth, A.: The Fire Modeling Intercomparison Project (FireMIP), phase 1: experimental and analytical protocols with detailed model descriptions, Geosci. Model Dev., 10, 1175–1197, https://doi.org/10.5194/gmd-10-1175-2017, 2017.

Raskutti, G., Wainwright, M. J., & Yu, B. (2014). Early stopping and non-parametric regression: an optimal data-dependent stopping rule. *The Journal of Machine Learning Research*, *15*(1), 335-366.

Satir, O., Berberoglu, S., & Donmez, C. (2016). Mapping regional forest fire probability using artificial neural network model in a Mediterranean forest ecosystem. *Geomatics, Natural Hazards and Risk*, *7*(5), 1645-1658.

Srivastava, N., Hinton, G., Krizhevsky, A., Sutskever, I., & Salakhutdinov, R. (2014). Dropout: a simple way to prevent neural networks from overfitting. *The journal of machine learning research*, *15*(1), 1929-1958.

Toms, B. A., Barnes, E. A., and Ebert-Uphoff, I.: Physically interpretable neural networks for the geosciences: Applications to Earth system variability, J. Adv. Model. Earth Syst., 12, e2019MS002002, https://doi.org/10.1029/2019ms002002, 2020.

Van Wagner, C. E.: Structure of the Canadian forest fire weather index, Can. For. Serv. Publ., 1333, 44 pp., 1974.

Van Wagner, C. E.: Development and structure of the Canadian forest fire weather index system, Canadian Forestry Service, Headquarters, Ottawa, Canada, Forestry Technical Report, vol. 35, 35 pp., 1987.

Verhegghen, A., Eva, H., Ceccherini, G., Achard, F., Gond, V., Gourlet-Fleury, S., & Cerutti, P. O. (2016). The potential of Sentinel satellites for burnt area mapping and monitoring in the Congo Basin forests. *Remote Sensing*, *8*(12), 986.

Vitolo, C., Di Giuseppe, F., Krzeminski, B., and San-Miguel-Ayanz, J.: A 1980–2018 global fire danger re-analysis dataset for the Canadian Fire Weather Indices, Scient. Data, 6, 190032, https://doi.org/10.1038/sdata.2019.32, 2019.

Ying, L., Cheng, H., Shen, Z., Guan, P., Luo, C., & Peng, X. (2021). Relative humidity and agricultural activities dominate wildfire ignitions in Yunnan, Southwest China: Patterns, thresholds, and implications. Agricultural and Forest Meteorology, 307, 108540.

Zhang, G., Wang, M., & Liu, K. (2021). Deep neural networks for global wildfire susceptibility modelling. *Ecological Indicators, 127,* 107735.

Zou, G.: Toward using confidence intervals to compare correlations, Psychol. Methods, 12, 399–413, https://doi.org/10.1037/1082-989X.12.4.399, 2007.

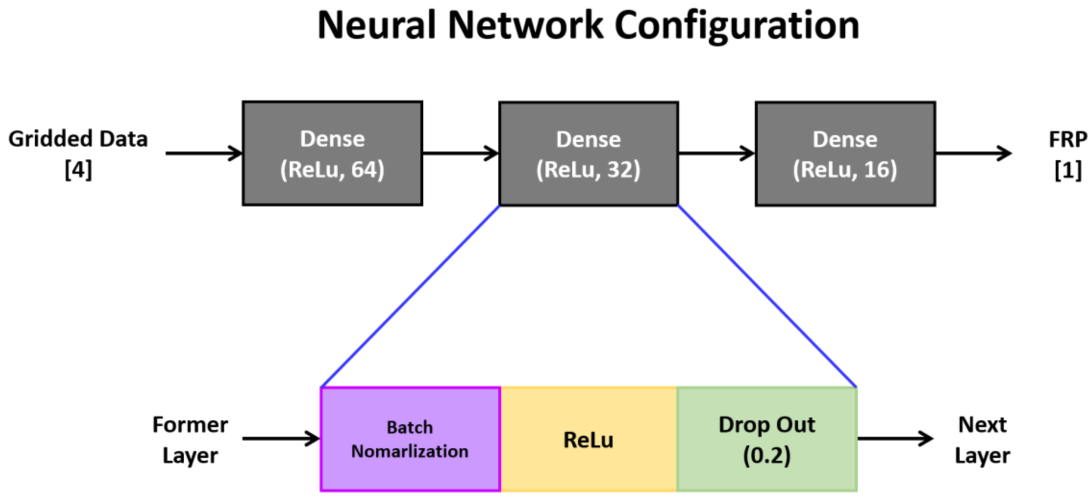

Figure 1. Configuration of the FFNNs.

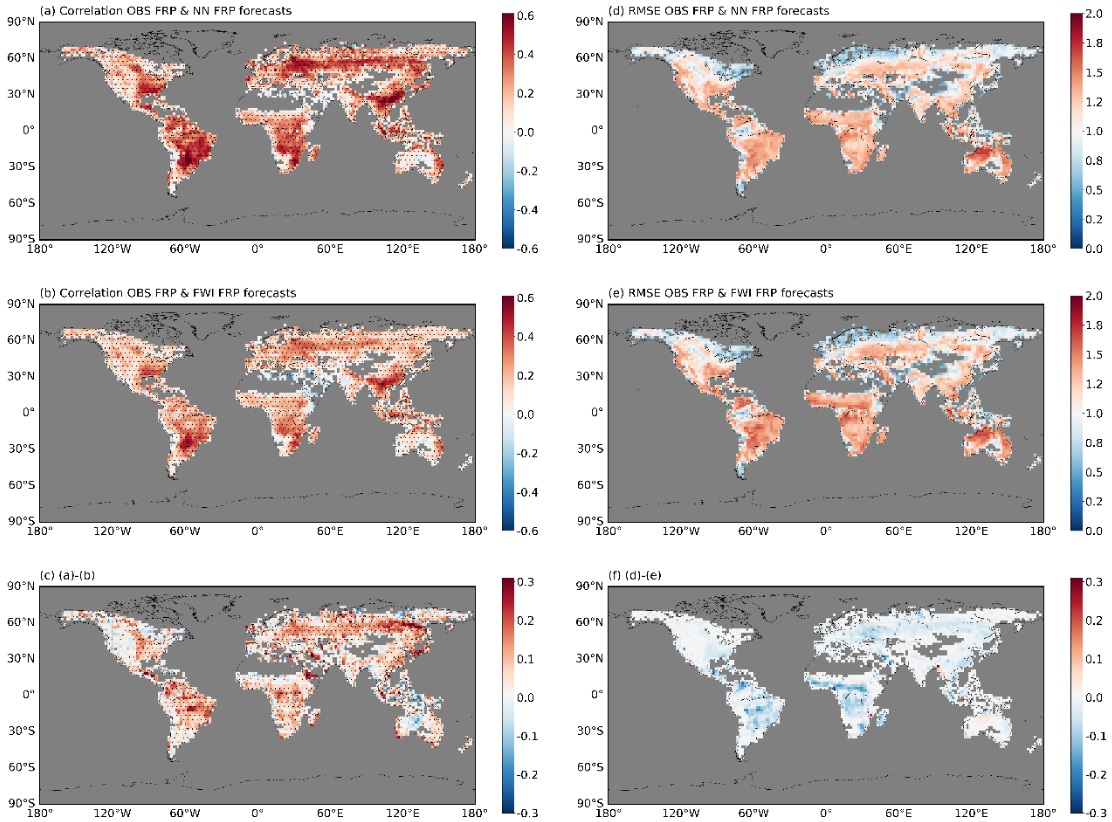

Figure 2. Correlation skill between the observed daily FRP and the estimated FRP values in (a) the FFNNs or (b) FWI-based model during 2001–2020. (c) Difference in the correlation skill in the FFNNs from that in the FWI-base model. RMSEs between the observed daily FRP and the estimated FRP values in (d) the FFNNs, or (e) FWI-based model during 2001–2020. (f) Difference in the RMSE in the FFNNs from that in the FWI-base model. The dots in panels (a) and (b) denote the grid points where the correlation skill exceeds a 95% confidence level based on the t-test; those in panel (c) denote the area whose correlation skill difference is above a 95% confidence level calculated as described by Zou (2007).

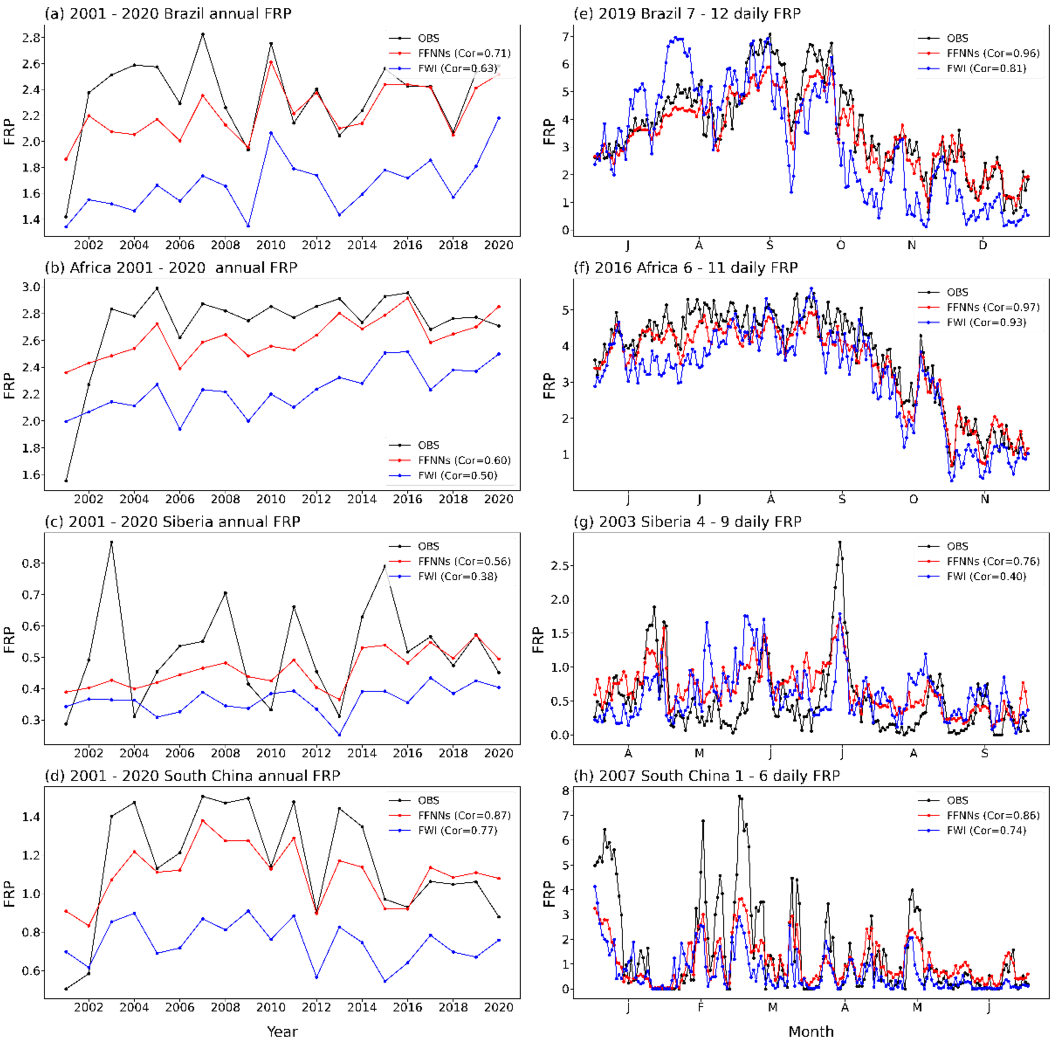

Figure 3. Time series of the annually-averaged (left) and daily (right) FRP in the observation (black), FFNNs (red), and FWI-based model (blue) over (a), (b) Brazil (64–40°W, 21–1°S), (c), (d) southern Africa (14–36°E, 18°S–6°N), (e), (f) Siberia (104–134°E, 48–60°N), and (g), (h) southern China (108–120°E, 22°N–30°N). Correlation coefficient between the observation and the FFNNs, and FWI-based model is denoted by the red, and blue in each panel, respectively.

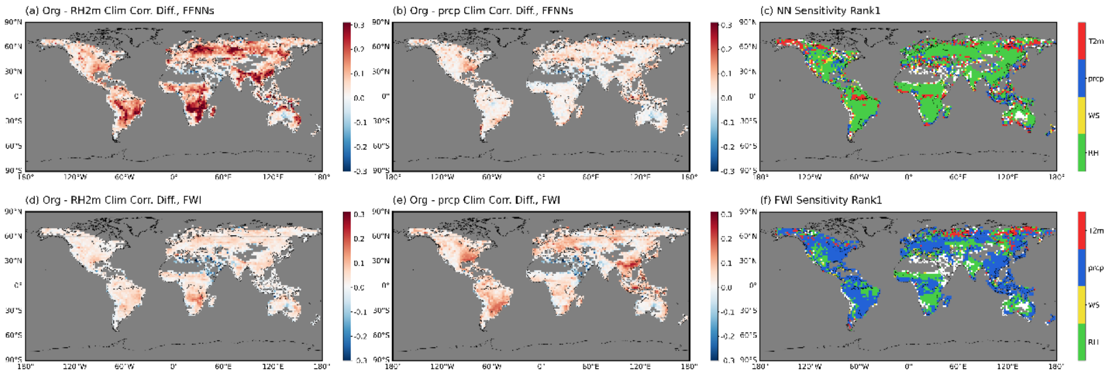

Figure 4. Difference in the correlation skill of the original FRP estimation in the FFNNs from that by prescribing (a) the RH2m or (b) the PRCP as the daily climatological values. (c) Spatial distribution of the meteorological variable where the decrease in correlation is largest by prescribing the climatological value. Panels (d), (e), (f) are the same as (a), (b), and (c) but for the FWI-based model. In panels (c) and (f), 2 m air temperature, PRCP, 10 m wind speed, and RH2m are indicated in red, yellow, green, and purple, respectively.

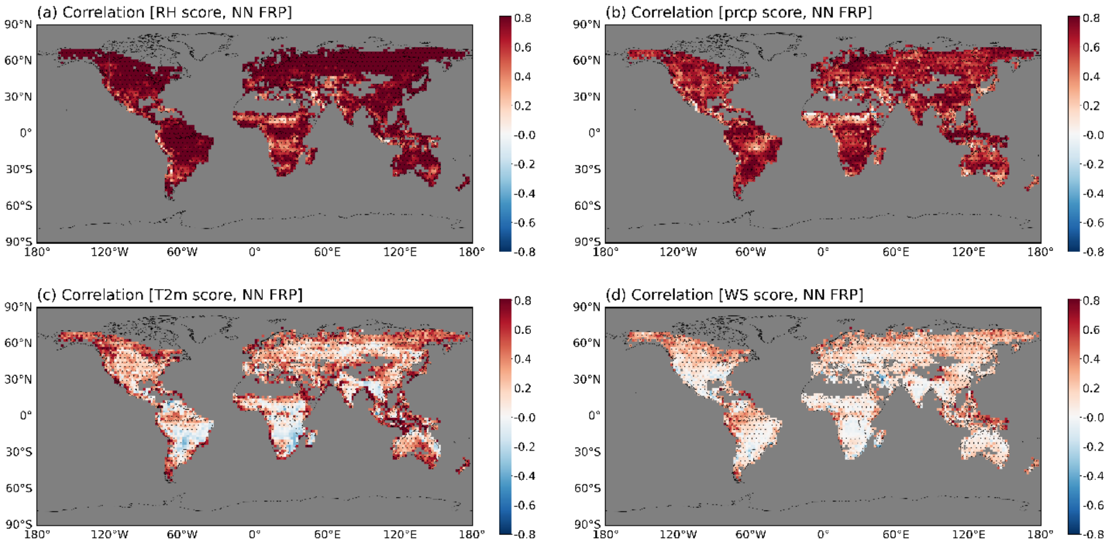

Figure 5. Correlation skill between the relevance score for each variables derived from layer-wise relevance propagation (LRP) and the estimated FRP in the FFNNs during the 2001–2020 period.

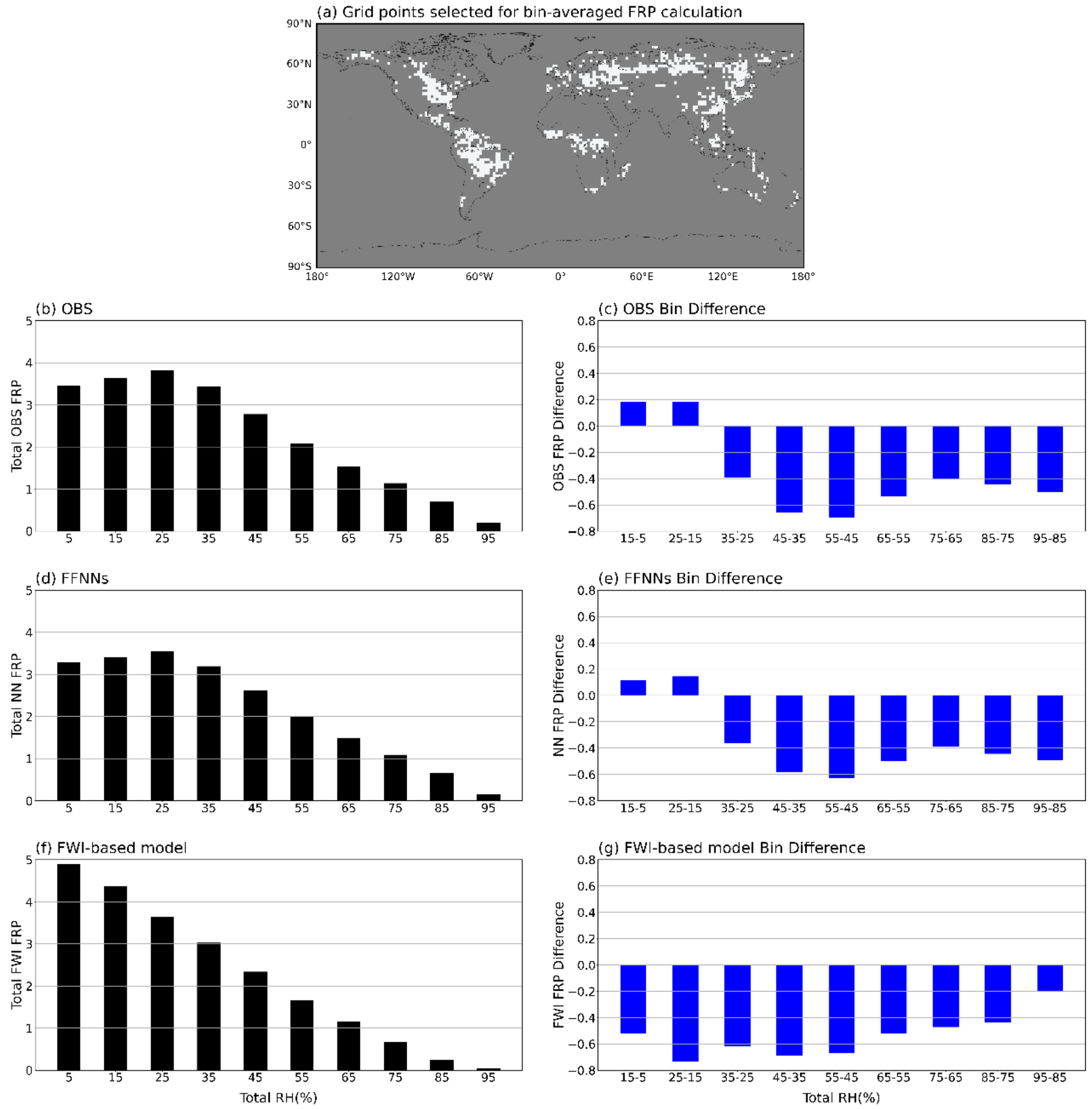

Figure 6. (a) Grid points selected for bin-averaged FRP calculation. Case-averaged FRP with respect to the RH2m with a 10% interval in (b) the observations, (d) FFNNs, and (f) FWI-based model. The figures illustrate the difference in the case-averaged FRP at the upper bin from the lower bin in (c) the observations, (e) FFNNs, and (g) FWI-based model.

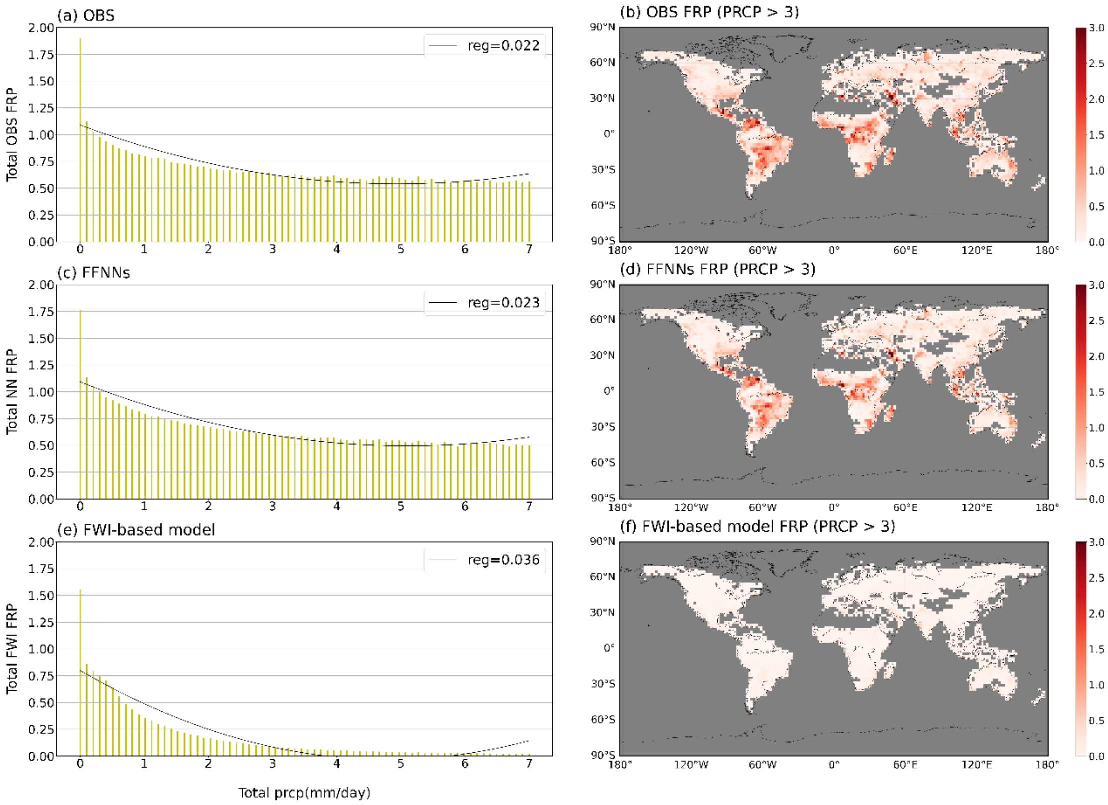

Figure 7. Case-averaged FRP with respect to the PRCP with 0.1 mm/day interval in (a) the observations, (c) FFNNs, and (e) FWI-based model. The black line in each panel quadratic shows the fitted line to the quadratic regression, and number in the upper right corner denotes the quadratic coefficients. The figures illustrate the spatial distribution of the case-averaged FRP when the PRCP > 3 mm/day in (b) the observations, (d) FFNNs, and (f) the FWI-based model. The selected areas for the calculation of the bin-averaged values is given in Figure 6a.